ChemPhotoChem

Research Article
doi.org/10.1002/cptc.202500191

Chemistry Europe
European Chemical Societies Publishing

www.chemphotochem.org

Tailoring the Film Thickness of Template-Assisted Sol–Gel-Derived Porous WO_3 Photoanodes for Highly Efficient Photoelectrochemical Water Oxidation

Lukas Max Mayer and Roland Marschall*

Photoelectrochemical hydrogen production is a promising and cost-effective strategy to provide clean and sustainable fuel. Due to its excellent electrical and optical properties, tungsten trioxide (WO_3) is one of the most studied electrode materials in this field, and it is well known that the incorporation of pores into the semiconductor can improve its photoelectrochemical performance. Using a facile and scalable template-assisted sol–gel technique, porous WO_3 thin films were tailored by simply varying the number of dip coating cycles. By crystallizing these films at 400 °C, a β-orthorhombic/γ-monoclinic crystal structure and an average surface area of 32 $m^2\ g^{-1}$ were obtained. By optimizing the layer thickness of these photoanodes on fluorine-doped tin oxide, photocurrents of up to 3.3 mA cm^{-2} at 1.23 V_{RHE} (in 0.1M H_2SO_4, pH = 0.71) were achieved without the use of any co-catalysts or sacrificial agents. Our photoelectrodes also showed highly reproducible photocurrents, and their high stability was proven in cycling tests, long-term measurement and post-photoelectrochemical characterization. Our work represents a very simple preparation optimization to achieve high-performing WO_3 photoanodes for photoelectrochemical applications.

1. Introduction

Due to the ongoing climate change, the number ofextreme weather events like forest fires, droughts, heat waves, storms, and inland and coastal floods increased during the last years.[1–4] To slow down this climate change, emission of greenhouse gases like CO_2 have to be reduced. To obtain this goal, the replacement of conventional energy carriers like fossil fuels by renewable and clean energy carriers is necessary. Hydrogen with its high gravimetric energy density of 33.3 kWh kg^{-1} is considered a promising clean alternative energy carrier.[5] Splitting H_2O into H_2 and O_2 using a photoelectrochemical (PEC) cell enables the environmentally friendly and cost-effective production of hydrogen. PEC devices utilize semiconductor photoelectrodes to directly convert solar energy into chemical energy, stored in form of hydrogen.[6–8]

The main challenge of PEC water splitting is to use earth-abundant, visible light absorbing, and inexpensive semiconductors for the efficient and cost-effective commercial production of hydrogen. This requires a solar-to-hydrogen efficiency above 10%, a photoelectrode lifetime of over 5000 h and production costs of \$2–\$4 kg^{-1} hydrogen.[9,10]

Various semiconductors have been explored since the first PEC cell using TiO_2 as an electrode material was developed by Fujishima and Honda in 1971.[11,12] Among them are metal oxides like $BiVO_4$,[13,14] Fe_2O_3,[15,16] and ZnO;[17,18] metal chalcogenides;[19] and metal nitrides.[20] Due to its earth abundance, the n-type semiconductor tungsten oxide (WO_3) is a widely used photoanode material in PEC water splitting.[21–23] It offers an indirect band gap of 2.5–2.8 eV, which enables the absorption of around 12% of the sunlight spectrum.[24,25] Compared to other common photoelectrode materials, like TiO_2 and hematite, it shows a better hole diffusion length (≈150 nm) and sufficient electron mobility (12 $cm^2\ V^{-1}\ s^{-1}$).[22,26] It is stable in acidic electrolytes (pH ≈ 0–4) and resistant against photocorrosion.[27,28] However, due to the limited absorption properties of WO_3, a relatively thick film is required, and the resulting long charge carrier diffusion pathway can lead to a significant amount of recombination.[16] Its theoretical maximum photocurrent density is limited to 4 mA cm^{-2} under Air Mass 1.5 Global (AM 1.5 G) sun illumination.[23,29] Even if the theoretical maximum photocurrent of 4 mA cm^{-2} were reached, a hydrogen conversion efficiency of 5.8% could be achieved at best. This is still lower than the 10% required for commercial applications. Therefore, WO_3 electrodes exhibit limitations regarding their performance in PEC water splitting. Due to this reason, the development of WO_3 photoanodes is driven for the utilization in highly active heterojunctions[30,31] or the oxidation of other molecules than water.[32]

Commonly applied strategies to overcome the drawbacks of WO_3 are the implementation of a dopant,[33,34] the creation of a heterojunction,[30] or the formation of a nanostructured electrode.[29,35] Using a hydrothermal route, Wang et al. fabricated a nanostructured electrode yielding a photocurrent density of 3.7 mA cm^{-2} which is the best performance reached for WO_3 electrodes reported to date.[29]

L. M. Mayer, R. Marschall
Department of Chemistry
University of Bayreuth
95447 Bayreuth, Germany
E-mail: roland.marschall@uni-bayreuth.de

Supporting information for this article is available on the WWW under https://doi.org/10.1002/cptc.202500191

The formation of a photoelectrode with porous architecture is a further strategy to improve the PEC performance by reducing the charge carrier diffusion pathway to the semiconductor/electrolyte interface in comparison to bulk photoelectrodes. An enhanced photocurrent can be attributed to the high specific surface area and a large number of active sites.[36,37] In addition, the semiconductors absorption properties can be improved due to light reflections and scattering within the porous structure.[16,38]

For the synthesis of porous photoelectrodes, techniques like hydrothermal growth, sol–gel synthesis, or atomic layer deposition are commonly applied.[37,39] To improve the PEC performance, gaining control over the pore size and morphology is crucial. This can, for example, be achieved by utilizing soft or hard templates which aggregate due to inter- and intramolecular forces, whereby a large number of different architectures can be realized.[40,41] The sol–gel synthesis using block-copolymers as soft templates represents a simple and inexpensive technique for the fabrication of photoelectrodes which can be easily scaled up for commercial production.[10] Using such a preparation technique, Hilliard et al. synthesized porous WO_3 photoanodes yielding photocurrents of 0.6 mA cm^{-2} at 1.23 V_{RHE}[42] applying Pluronic P123 as template for the formation of the mesoporous structure of the photoanodes.

In this work, we optimized the performance of sol–gel-derived porous WO_3 thin-film photoanodes by tailoring their porosity and film thickness. Porous WO_3 photoanodes with an optimized thickness of 3.0 µm exhibited a maximum photocurrent of up to 3.3 mA cm^{-2} at 1.23 V_{RHE} under AM 1.5 G illumination in sulfuric acid, without the application of any cocatalysts or sacrificial agents. This value corresponds to 82% of the theoretical maximum value for WO_3. Our very simple approach is highly reproducible, and the photoelectrodes exhibit high stability over the course of cycling photocurrent measurements, making this method a promising and easy synthesis for high-performing WO_3 photoanodes.

2. Experimental Section

2.1. Materials

Acetone (Fisher Scientific ≥ 99.8%), ethanol (VWR, ≥99.93%), 2-propanol (VWR, ≥99.5%), Pluronic P123 (31000 g mol^{-1} Aldrich), tetrahydrofuran (Fischer scientific, ≥99.8%), and WCl_6 (abcr, 99.9%) were used without further purification. Fluorine doped tin oxide (FTO) substrates (Pilkington TEC 8 glass with a resistance of 8 Ω mm^{-2}) were bought from XOP-Glass. The substrates were cleaned using an ultrasonic bath in ethanol, acetone and isopropanol, followed by ultrapure water for 30 min each. Subsequent to this treatment, the FTOs were dried using nitrogen.

2.2. Synthesis WO_3 Photoanodes

In a typical synthesis to obtain porous WO_3 photoanodes, 0.9 g of Pluronic P123 are dissolved in a mixture of 40 ml of ethanol and 14.5 ml of THF. While stirring the solution, 9 g WCl_6 are added at once. The reaction mixture is stirred for 1 h and covered with a Parafilm during this period, the sol–gel solution changes its color from orange-brown to turquoise-blue.

Once the reaction is finished, the solution is dip-coated onto the FTO substrate. A dipping speed of 162 mm min^{-1} and a dwell time of 3 s are chosen (**Figure 1**). After each coating step, the photoanode is dried on a heating plate at 150 °C (2 min) followed by 300 °C (2 min). This cycle is repeated for 5, 10, 12, 13, and 15 times for the respective photoanodes. To ensure reproducibility, six photoanodes were fabricated for each number of dip coating cycles. During the coating step, the backside of the substrate is covered with Kapton tape which is removed prior to the annealing step. After finishing the coating, the photoanodes are calcined on a heating plate at 400 °C for 30 min.

2.3. Characterization Methods

2.3.1. Material Characterization

The cross section and morphology of the samples were investigated using field emission scanning electron microscopy (FESEM). Images were acquired with a Zeiss Leo 1530 with an acceleration voltage of 3 kV. The instrument was equipped with an SE2 and InLens detector. A working distance of 6–8 mm and a 30 µm aperture was applied.

For the Brunauer–Emmett–Teller (BET) analysis, an ASIQ-MP-MP-AQ physisorption analyzer from Anton Paar Quanta Tec

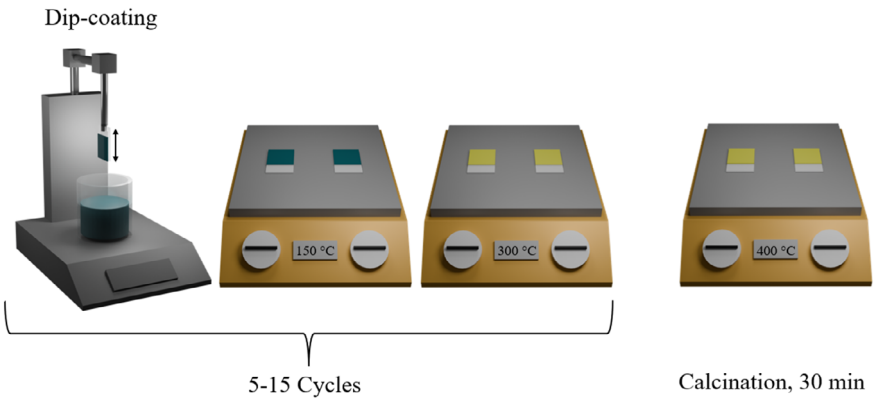

Figure 1. Schematic illustration of the applied sol–gel synthesis.

Inc. was used. The samples were dried for 12 h at 120 °C under vacuum prior to the measurements. All measurements were conducted using Krypton at 77 K under a constant p_0 of 2.63 Torr. For the multi-point BET analysis, the software ASiQwin from Quanta Chrome was utilized.

Crystal structure and phase of the WO_3 were investigated by X-ray diffraction (XRD) using a Rigaku Smart Lab diffractometer with a HyPix-3000 high energy resolution 2D HPAD detector at 20 °C and atmospheric conditions. The diffractograms were acquired in a range from 10 to 70° 2θ with a step width of 0.01° and a scan speed of 10° min^{-1}. A voltage of 45 kV and a current of 20 mA were applied at the anode. Copper Kα radiation with a wavelength of $\lambda = 1.54178$ Å was emitted from a rotating anode. For the measurements, grazing incidence XRD (GI-XRD) was applied.

For the acquisition of Raman spectra, a Horiba Jobin Yvon Raman spectrometer, equipped with an Olympus BX41 microscope was used. To deliver the incident radiation, a He-Ne-Laser with a wavelength of $\lambda = 633$ nm and a power of 11.5 mW was applied. The spectral measurement range was set between 50 and 2000 cm^{-1}. An accumulation number of 20 and an exposure time between 1 s and 2 s were chosen. Labspec software was used to record the spectra.

Ultraviolet-visible (UV-Vis) spectroscopy was conducted using a Perkin Elmer Lambda 750 spectrometer with a 100 mm Ulbricht sphere and an InGaAs detector. The spectra were obtained in a range from 200 nm to 800 nm with a step width of 1 nm. Reflectance spectra were acquired for the photoelectrodes and converted into pseudo-absorption after Kubelka-Munk. To determine the band gaps, the Tauc-plot method was applied.

For the acquisition of IR spectra, an Alpha II diffuse reflectance infrared Fourier transform spectrometer (DRIFT) from Bruker was utilized. The spectra were measured with a resolution of 4 cm^{-1} in a range from 4000 to 350 cm^{-1} performing 24 scans per measurement. The spectroscopy software OPUS from Bruker was used for the measurements.

2.3.2. Photoelectrochemical Measurements

All photoelectrochemical measurements were recorded with a Zahner Zennium CIMPS-PCS potentiostat. Thales Z 3.05 was the software used to acquire the data. The PEC cell, purchased from Zahner, has an irradiation window of 1 cm^2 and a three-electrode setup with a Pt-wire as the counter electrode and an Ag/AgCl (3 M NaCl) electrode as the reference electrode. The tungsten oxide photoanodes serve as the working electrode. The cell was either filled with a 0.2 M KH_2PO_4 (pH = 1.75) or a 0.1 M H_2SO_4 (pH = 0.71) electrolyte.

For the chopped light voltammetry (CLV) a Quantum Design LOT sun simulator, which was equipped with a 300 W Xe lamp and an AM 1.5 G filter, was applied. The power of the incident radiation reaching the PEC cell was set to 100 mW cm^{-2}. All measurements were performed in a range from 1.2 $V_{Ag/AgCl}$ to 0.15 $V_{Ag/AgCl}$. A scan speed of 5 mV s^{-1} and a light period time of 20 s were selected. 10 points were acquired per second. The measurements were performed using backside illumination.

For the incident photon to current efficiency (IPCE) determination, a Zahner TLS 03 was employed which was controlled using a Zahner PP211. Those measurements were acquired in a wavelength range from 300 to 800 nm. The illumination time was set to 10 s with a frequency of 1 Hz and a power of 95%. A voltage of 1.23 V_{RHE} was chosen, and the sample was irradiated from the front side.

To investigate the long-term stability of the synthesized WO_3 photoanodes, chronoamperometric measurements were performed. Therefore, an external bias was applied to the sample for 2 h while illuminating it with AM 1.5 G radiation. The photocurrent was acquired using a 0.1 M H_2SO_4 electrolyte (pH = 0.71).

The charge separation and injection efficiency were calculated according to Dotan et al.[43] Therefore, CLV measurements using 0.1 M H_2O_2 in 0.1 M H_2SO_4 were carried out. The photocurrents were recorded directly after adding the hole scavenger to the electrolyte. For the calculation of the charge carrier separation and injection efficiencies, Equation (1) and (2) were utilized.

$$J_{H_2O} = J_{abs} \times P_{sep} \times P_{inj} \quad (1)$$

$$J_{H_2O_2} = J_{abs} \times P_{sep} \quad (2)$$

The value for J_{abs} was chosen as 4 mA cm^{-2} according to Wang et al.[29] Other values which contribute to these equations are J_{H_2O} (photocurrent density in water), P_{sep} (charge separation efficiency), $J_{H_2O_2}$ (photocurrent density with the sacrificial agent H_2O_2), P_{inj} (charge injection efficiency), and J_{abs} (total photocurrent density due to absorbed photons).

3. Results and Discussion

Photoanode optimization was performed by applying multiple dip coating cycles. To determine the influence of the number of dip coating cycles on the amount of semiconductor attached to the substrate, the samples are being weighed (Table S1, Supporting Information). The sample mass increases steadily from five cycles (2.5 ± 0.2 mg) to 15 cycles (11.2 ± 0.1 mg). Only photoanodes with 13 cycles do not follow this trend (**Figure 2**). They just exhibit an average amount of 8.5 ± 0.2 mg, while the samples synthesized by applying 12 dip coating cycles already displayed a mass of 9.8 ± 0.1 mg.

Since WO_3 shows limited absorption properties, the layer thickness of the photoanodes is an important property.[44] If the films are too thin, a sufficient light absorption is not achieved, whereas too thick films exhibit increased charge carrier recombination. Cross-sectional SEM images are used to determine the thickness of the porous WO_3 photoanodes (**Figure 3**a–e and Table S2, Supporting Information). Those values show a steady increase of the film thickness with the amount of coating cycles performed. While the five cycle sample exhibits a thickness of 1.8 μm, the one fabricated by performing 15 cycles has a thickness of 5.6 μm. An increase can also be noticed if the amount of coating steps is increased from 12 (2.9 μm) to 13 (3.0 μm) cycles,

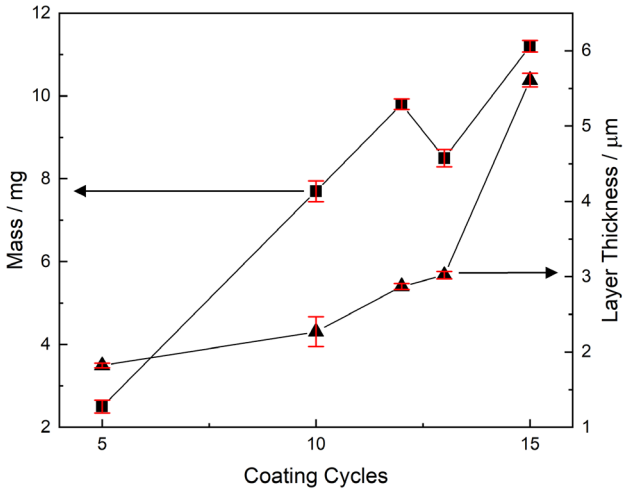

Figure 2. Average sample mass and layer thickness plotted against the number of coating cycles performed.

even though the mass reduces from 12 to 13 cycles. As these data show a correlation between the number of cycles performed and the film thickness, the samples are named by their layer thickness in the following.

To investigate the surface of the photoanodes, top-view SEM images were acquired (Figure 3f–j). These show a porous morphology for all samples. Every investigated photoelectrode exhibits large pores on the scale of a few hundred nanometers. Their extent and number do not change with an increasing layer thickness of the WO_3. The Kr physisorption data (Table S3, Supporting Information) show a surface area between $29.5 \pm 3.2\ m^2\ g^{-1}$ and $32.7 \pm 2.1\ m^2\ g^{-1}$. Therefore, the surface area does not depend on the layer thickness. While the highest surface area can be obtained for samples with a thickness of 1.8 µm, samples with a layer thickness of 2.9 µm exhibit the lowest surface area. Although these deviations are not significant, they could be an indication for the PEC performance of these electrodes, as the surface area strongly influences the length of the required charge carrier diffusion pathway and the number of catalytic active sites. In addition, the light absorption should be better for a material with higher porosity, due to reflection and scattering of the incident light inside the pores.[36]

Amer et al. published a comparable sol–gel based dip-coating approach for WO_3 photoanodes using the di-block copolymer PEO117-b-PS198 as a template. They added WCl_6 into a mixture of EtOH and HCl. By applying 13 coating layers on the substrate, they obtained a layer thickness of 1.42 µm, which is much lower than the values reached by our synthesis. A reason could be the lower concentration of the precursor solution used by Amer et al. Although their photoelectrodes show a similar surface area than the ones synthesized here, they just yield a photocurrent of 0.58 mA cm^{-2} at 1.23 V_{RHE} (measured in 0.5 M Na_2SO_4 electrolyte).[45]

From GIXRD measurements, the diffraction patterns show reflections of monoclinic (ref: 01-072-1465) and orthorhombic (ref: 01-071-0131) WO_3 phase (**Figure 4**a and S1, Supporting Information). This suggests that the material adopts a distorted β-orthorhombic/γ-monoclinic structure, which corresponds to the results of Hilliard et al.[42] While the monoclinic modification crystalizes in a P2/1n space group, the orthorhombic one forms a Pmnb space group. The three main reflections of the WO_3 semiconductors are located at 2θ values of 23.2°, 23.7,° and 24.2°, and correspond to the (002), (020), and (200) lattice planes of WO_3. The intensity distribution of those three reflections allows for an estimation of the enrichment of a certain facet at the surface of the photoelectrode. Most samples show nearly the same intensity for the reflection of the (002) plane, which is said to be the most active facet towards water oxidation, and the (200) reflection.[21,23,46] Nevertheless, some samples exhibit a preferential enrichment of the (200) facet, in comparison to the (002). An example is shown in the diffraction pattern of the sample with 2.3 µm thickness. The reflection of the (020) plane is the least pronounced for every sample, making it the least exposed facet at the surface.

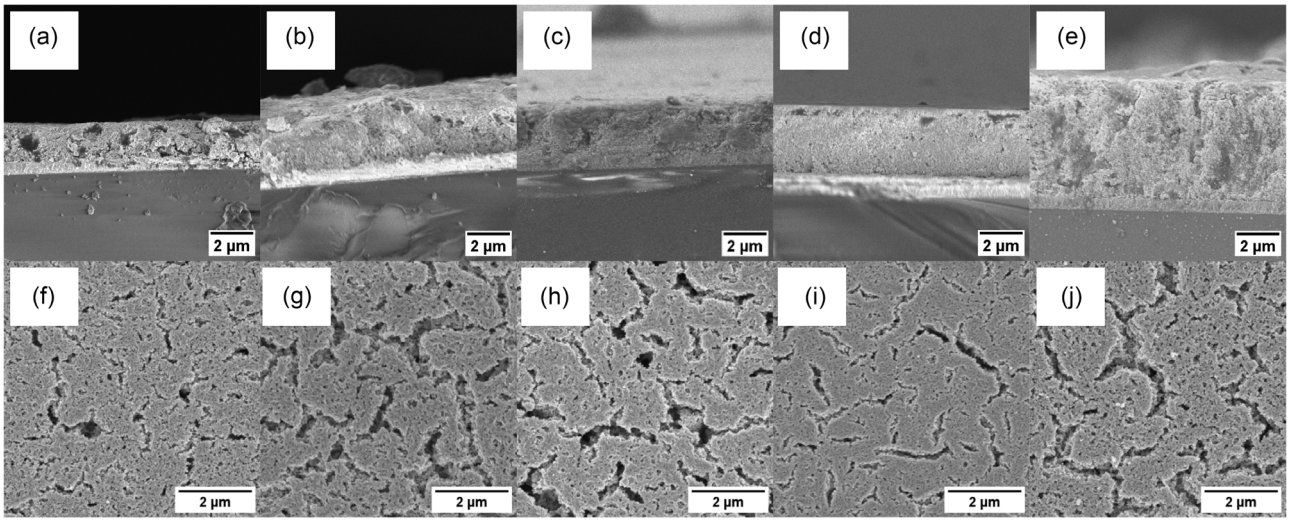

Figure 3. a–e) Cross-sectional and f–j) top-view SEM images of the samples synthesized by performing 5, 10, 12, 13, and 15 dip coating cycles. SEM = scanning electron microscopy.

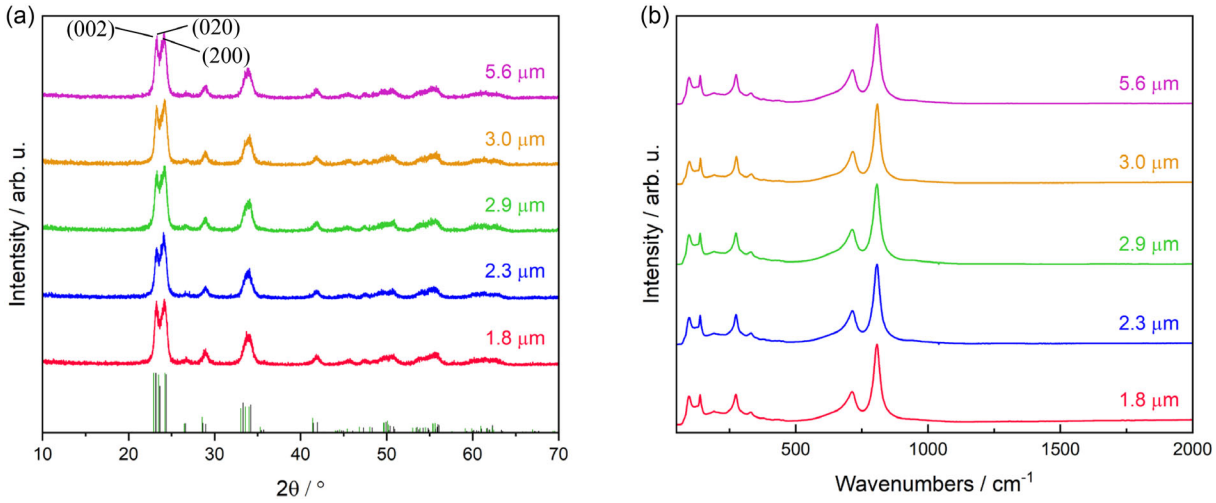

Figure 4. a) Diffraction patterns of the porous photoanodes, references: monoclinic WO_3 black (ref: 01-072-1465) and orthorhombic WO_3 green (ref: 01-071-0131). b) Raman spectra of the synthesized photoanodes.

Analyzing the Raman spectra, signals of the orthorhombic and the monoclinic phase of WO_3 can be assigned (Figure 4b and S2, Supporting Information). In these spectra, two main peaks are present at Raman shifts of 807 and 713 cm^{-1}. Those can be correlated to the stretching of ν (O—W—O) and occur at the same wavenumbers for both WO_3 phases. The bending of the δ (O—W—O) bonds is responsible for the peaks at 328 and 269 cm^{-1}. Further signals occurring at Raman shifts of 191, 138, and 96 cm^{-1} belong to lattice vibrations of the crystal. The peak at 96 cm^{-1} is characteristic of the orthorhombic phase of WO_3. The shoulder which is located at 81 cm^{-1} corresponds to the monoclinic modification.[47–49] Due to the fact that the peak at 713 cm^{-1} exhibits a shoulder at lower wavenumbers, the photoelectrode material is not perfectly crystalline. The assumption can be made that a certain amount of amorphous WO_3 is present.[50] The Raman spectra show the same signals for all synthesized samples, which indicates a high reproducibility of the applied synthesis.

Comparing the UV-Vis spectra of the photoanodes with different layer thicknesses, no increase of the absorption can be observed for the samples with a thicker semiconductor film (Figure S3 and S4, Supporting Information). Only a few samples exhibit an increased absorption, in comparison to the other photoanodes. The absorption edges of all photoanodes are located between 455 and 465 nm. Those are in line with the literature values for WO_3.[21] Photoanodes with a thickness of 1.8 µm exhibit the lowest absorption edge of 455 nm, while the ones for the thicker films are hardly shifted to higher wavelengths.

By applying the Tauc-plot method, a slightly decreasing bandgap can be determined with an increasing thickness of the photoanodes (**Figure 5**a; Table S4 and S5, Supporting Information). With a value of 2.78 eV, the highest bandgap can be obtained for samples with a thickness of 1.8 µm, while the ones with 3.0 µm just exhibit a bandgap of 2.67 eV. Therefore, the thicker samples are able to utilize a slightly larger share of the incident sunlight. These changes are however within the error

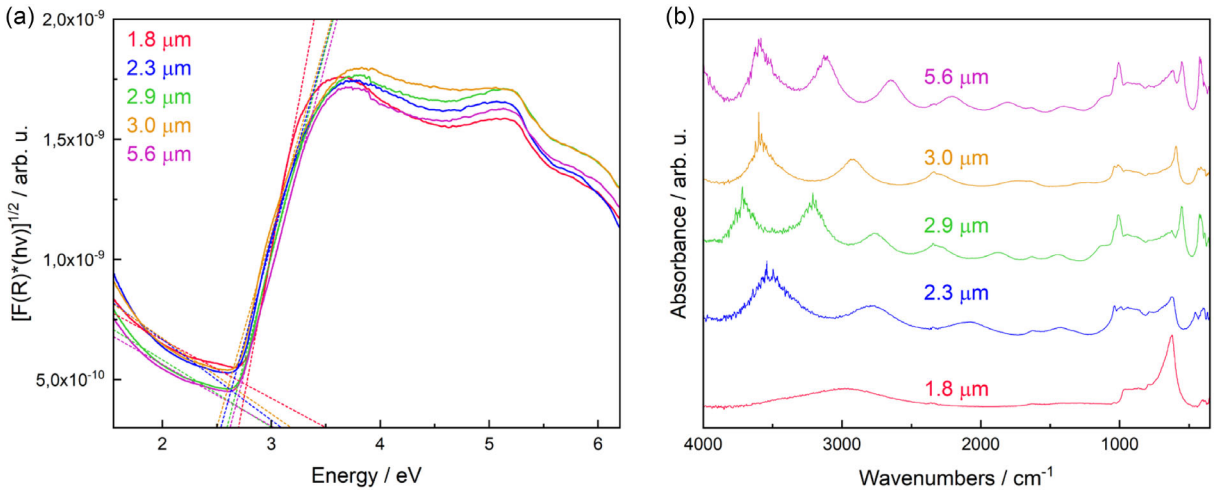

Figure 5. a) Tauc-plot and b) DRIFT spectra of the porous WO_3 photoanodes with a layer thickness of 1.8, 2.3, 2.9, 3.0, and 5.6 µm.

range of the Tauc-method. They can be attributed to variations of the film's thickness and defects.

Upon analyzing the DRIFT spectra, the characteristic signals of WO_3 can be identified as well (Figure 5b and S5, Supporting Information). While the peak at a wavenumber of 1040 cm^{-1} is attributed to the W—OH bond, the peak at 995 cm^{-1} can be assigned to vibrations of the W═O bonds. A broad band in the range from 600 to 700 cm^{-1} can be correlated with the W—O—W vibrations.[51,52] Another peak, whose intensity and shift varies slightly, is present at in the range from 560 to 630 cm^{-1}. This signal represents the amount of amorphous WO_3 in the photoanode, but is very difficult to analyze.[53,54] In addition, those spectra show that the template was removed successfully. If residues of the template Pluronic P123 would be present, they would exhibit signals at 2850 and 2970 cm^{-1}.[55]

3.1. Photoelectrochemical Measurements

To examine the performance of the porous photoanodes, CLV measurements were conducted. First, we used a KH_2PO_4 buffer (pH = 1.85) electrolyte for those measurements. It is known that higher photocurrent densities can be achieved in an H_2SO_4 electrolyte, nevertheless we wanted to investigate milder conditions first in order to examine molecular catalyst in the future. Therefore, the first objective was to optimize the WO_3 performance in a KH_2PO_4 electrolyte. To analyze the stability of these electrodes, three consecutive CLV measurements were performed.

The CLV measurements exhibit a general trend of an increasing average and maximum photocurrent density with a higher layer thickness (**Figure 6**a and S6−10; Table S6–S10, Supporting Information). A maximum value is reached for the photoanodes with a thickness of 3.0 µm. Those yield a maximum photocurrent density of 3.1 mA cm^{-2} at 1.23 V_{RHE} (Figure 6b). This value corresponds to 78% of the maximum possible value for WO_3 photoanodes. Within the batch of photoanodes with a layer thickness of 3.0 µm the photocurrent only varies slightly. After the maximum, a slight decrease of the PEC performance can be recognized for photoanodes of 5.6 µm thickness, although this decrease is not significant. The photoanodes with a layer thickness of 2.9 µm are not in line with this trend and exhibit the lowest photocurrents of all samples. Cross sectional SEM images of these samples could provide a possible explanation for their low photocurrent and IPCE values (Figure S11, Supporting Information). Within the WO_3 layers some darker parts can be identified. Those could be caused by residues of the polymer template, as indicated by their lower surface area. Due to the DRIFT measurements being surface sensitive, those spectra do not show any signals of template residues.

Regarding the onset potential of the photoanodes, no change can be recognized for the different layer thicknesses. It is located at a value of 0.47 V_{RHE} for all samples. Additionally, the fill factor of the CLV curves shows no relation to the layer thickness of the semiconductor. The transients of the photocurrent measurements are always flat, indicating a good electron transfer at the surface.

By analyzing the development of the photocurrent over three CLV measurements, an average decrease of 0.11 mA cm^{-2} can be recognized (Figure S12, Supporting Information). For the samples with a layer thickness of 3.0 and 5.6 µm, the second measurement is even better than the first one, although the improvement is not significant. With a decline of only 3% (0.06 mA cm^{-2}), samples with 3.0 µm thickness retain most of their performance over three measurements, which indicates a good stability of those photoelectrodes.

Analyzing the IPCE values of the photoanodes, values of up to 55.4% (at 318 nm) can be determined for the 1.8 µm photoanodes (**Figure 7**a and S13; Table S11, Supporting Information). These high values indicate an efficient charge transport within the semiconductor although their thin layer limits the absorption. With maximum IPCE values of 49.8% (at 339 nm), the photoanodes with a layer thickness of 3.0 µm exhibit a slightly lower external quantum yield. The wavelength at which the maximum IPCE value is measured changes with the layer thickness. While it is located below 340 nm for samples of 1.8 and 3.0 µm thickness, photoanodes with a thickness of 2.3, 2.9, and 5.6 µm show a shift

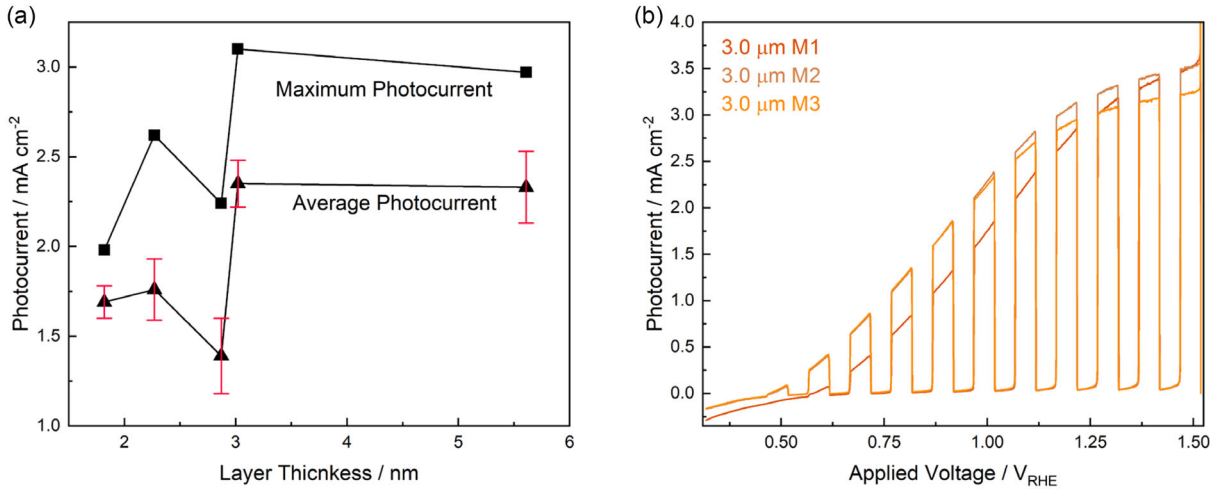

Figure 6. a) Average (of the 1st measurement) and maximum photocurrent values of all porous photoelectrodes at 1.23 V_{RHE}. b) CLV measurements of a 3.0 µm thick electrode, consecutive measurements were conducted in a KH_2PO_4 buffer.

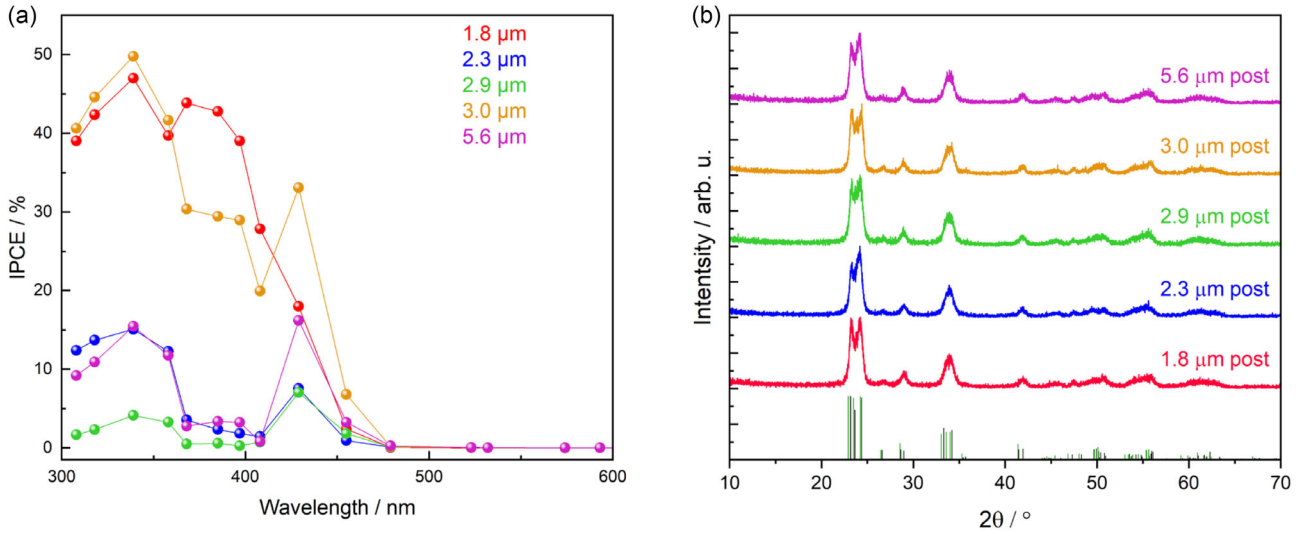

Figure 7. a) IPCE measurements of porous photoanodes with a layer thickness of 1.8, 2.3, 2.9, 3.0, and 5.6 µm and b) X-ray diffractograms of the same photoanodes, acquired after the PEC measurements, references: monoclinic WO_3 black (ref: 01-072-1465) and orthorhombic WO_3 green (ref: 01-071-0131).

of the wavelength to higher values. These electrodes are not able to utilize the high energetic part of the solar spectrum efficiently. This could be one reason for their lower photocurrent values.

The PEC measurements lead to the conclusion that the samples with a layer thickness of 3.0 µm exhibit the best photocurrent density due to the combination of an efficient charge carrier diffusion within the semiconductor and a sufficient absorption due to the optimized layer thickness. A further increase of the layer thickness leads to a higher charge carrier recombination. The thinnest films, which show the best charge carrier transport capabilities, lack the ability to absorb enough of the incident light.

By acquiring X-ray diffractograms after the photoelectrochemical measurements, the stability of the photoelectrode material is investigated (Figure 7b). These diffractograms do not exhibit any differences in comparison to the ones acquired prior to the PEC measurements. Neither the crystal facet enrichment nor the phase composition changes. This proves the structural (photo)stability of the photoelectrodes.

To yield the maximum possible photocurrent density, another six photoanodes with a layer thickness of 3.0 µm were synthesized and measured in a 0.1 M H_2SO_4 electrolyte. Those electrodes showed the same material characteristics as the ones characterized before. The distorted β-orthorombinc/γ-monoclinic crystal structure can be determined by the XRD and Raman measurements (Figure S14, Supporting Information). They further exhibit an average band gap of 2.71 eV, which is in line with the results of the first synthesis (Figure S15a, Table S12, Supporting Information). In addition, the DRIFT spectra show no signals of polymer residues (Figure S15b, Supporting Information). Their surface area was determined to a value of 32 m^2 g^{-1}.

These photoanodes measured in the H_2SO_4 electrolyte (Figure S16 and Table S13, Supporting Information) yield photocurrents up to a value of 3.3 mA cm^{-2} at 1.23 V_{RHE}, which corresponds to 82% of the theoretical maximum value for WO_3 (**Figure 8**a). This remarkable value exceeds many of the photocurrent densities reported for bare WO_3 photoanodes in the

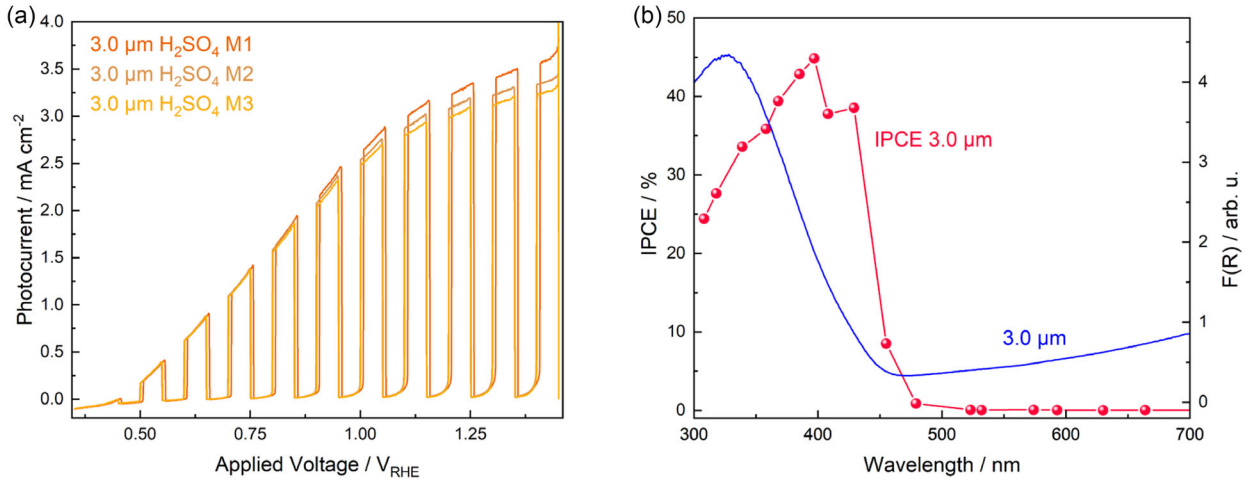

Figure 8. a) CLV measurements of the best 3.0 µm photoanode, measured in H_2SO_4, b) IPCE value of a 3.0 µm photoanode, measured in H_2SO_4, compared with its Kubelka–Munk function.

literature.[21,23] The groups of Augustynski and Park both also prepared porous WO_3 photoanodes.[56,57] They were using polyethylene glycol (PEG) instead as a template, both applying a drop-casting technique rather than a homogeneous dip-coating approach. Furthermore, a peroxy-tungstate precursor solution is formed by dissolving W powder in hydrogen peroxide, and 2-propanol is used as a solvent. While Augustynski et al. just reach a layer thickness of 2.5 µm, Park et al. yield a maximum photocurrent of around 3 mA cm^{-2} at 1.23 V_{RHE}, although these measurements were carried out in a 1 M H_2SO_4 electrolyte.

A further sol–gel synthesis route for porous WO_3 photoanodes was presented by the group of Norimatsu.[58] They also utilized PEG as a template, and tungstic acid was used as a precursor dissolved in a 30% ammonia solution and EtOH as a solvent. A doctor-blade technique was applied for the synthesis of the films. Measuring in a 1 M $HClO_4$ solution, these electrodes yielded a photocurrent of up to 3 mA cm^{-2} at 1.23 V_{RHE} as well. In both cases, much higher electrolyte concentrations and complex precursors are used in contrast to the presented results.

The 3.0 µm photoanodes measured in H_2SO_4 show IPCE values of just 44.8% (at 397 nm), which indicates a potential for a further improvement of their performance (Figure S17a and Table S14, Supporting Information). This can be confirmed by the comparison of the Kubelka-Munk function and the IPCE curve (Figure 8b). While the maximum external quantum yield is observed at 397 nm, the maximum absorption is located at a wavelength of 330 nm. Therefore, photons at this wavelength cannot be converted that efficiently. Improving the efficiency of those photoelectrode in the high energetic range could improve their already impressive performance even further in the future.

To compare the measured photocurrents with the theoretical ones, the IPCE measurements are integrated according to Patzke et al.[59] For this determination, the IPCE spectra of the best photoanodes (measured in KH_2PO_4 and H_2SO_4) are integrated in the range of the bandgap of WO_3 and compared to the AM 1.5 G spectrum (Figure S18, Supporting Information), while the WO_3 electrodes can only utilize 29% of the incident light when the KH_2PO_4 buffer is utilized, by changing the electrolyte to 0.1 M H_2SO_4 35% of the incident photons can be used for water oxidation. If the theoretical photocurrent is calculated according to these integrations, the results are lower than the measured photocurrents. This deviation can originate in the use of a different light source for the IPCE spectra than for the CLV measurements. Furthermore, IPCE is only measured at certain wavelengths and not under AM 1.5 G illumination. Therefore, charge carrier separation can be another property that need to be investigated.

To calculate the charge separation and injection efficiency, according to Dotan et al., measurements using a H_2O_2 hole scavenger were performed for the best photoanodes (**Figure 9**a).[43] The application of the hole scavenger increases the photocurrent from 3.06 to 3.34 mA cm^{-2} at 1.23 V_{RHE}. Those measurements exhibit for values of 84% the charge separation efficiency and 92% for the charge injection efficiency, which are both very good compared to literature.[60,61] A further measurement was carried out using MeOH as a hole scavenger, exhibiting a maximum photocurrent of 6.82 mA cm^{-2} at 1.23 V_{RHE}, but of course the photocurrent doubling caused by MeOH must be considered (Figure S19, Supporting Information).

While the XRD patterns acquired after the photoelectrochemical measurements already showed structural stability, the photochemical stability of the electrodes must be proven by performing long-term measurements (Figure 9b). Those stability tests were carried out under AM 1.5 G illumination and the application of a bias of 1.23 V_{RHE} for 2 h. During the measurement time, a 27.9% loss of the photocurrent could be recognized, which is most likely due to surface reconstruction forming the actual catalytic surface.[62] By detecting the amount of oxygen produced during this period (256.4 µL), the Faradaic efficiency was calculated to a value of 21.7%. Faradaic efficiency is actually rarely reported for WO_3 photoanodes, it exhibits a challenge of porous WO_3 photoanodes. Oxygen bubbles formed within the pores of the electrode have to be transported to the bulk electrolyte to be measured. Those mass transfer limitations could be an

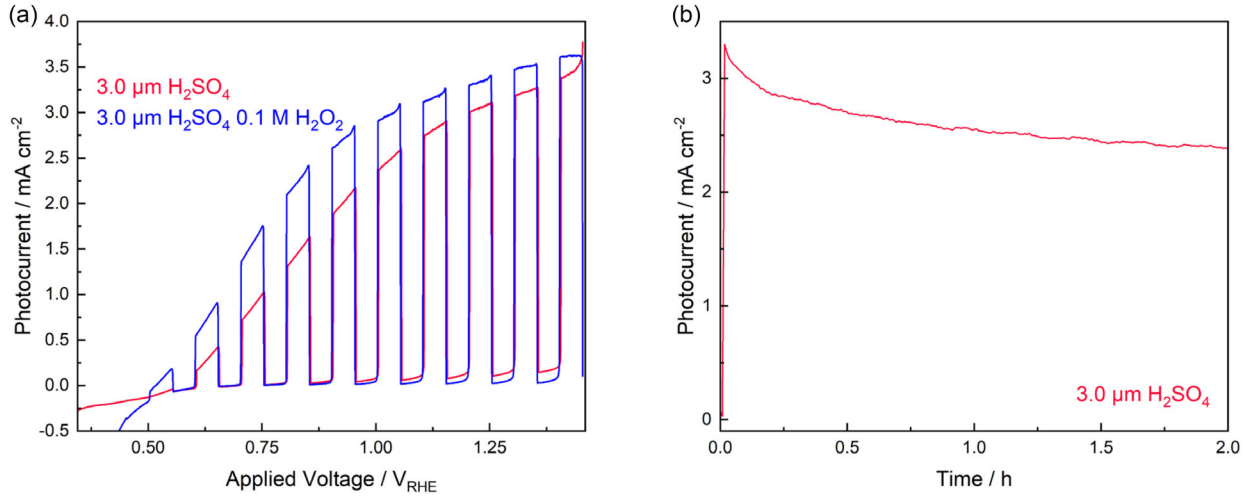

Figure 9. a) CLV measurement of a 3.0 µm photoanode in 0.1 M H_2SO_4 without and with the addition of 0.1 M H_2O_2. b) Photostability measurement for 2 h under an applied bias of 1.23 V_{RHE}.

explanation for the low faradaic efficiency values. Additionally, we observed accumulation of gas bubbles at the surface of the photoelectrodes which deteriorates the semiconductor-electrolyte contact. This is one reason for the decline of the photocurrent. Another reason could be the formation of peroxo species during the reaction which is a common issue for WO_3.[23,62]

4. Conclusion

In summary, we have prepared porous WO_3 photoanodes by applying a simple dip-coating technique which can be easily scaled up. Those electrodes show a surface area of 31.5 m^2 g^{-1} and form a distorted β-orthorombinc/γ-monoclinic crystal structure. By tailoring the film thickness to a value of 3.0 µm, photocurrent densities of up to 3.1 mA cm^{-2} at 1.23 V_{RHE} were reached in KH_2PO_4 electrolyte. The small mean square displacement of the photocurrent mean value of only 6% indicates a high reproducibility of these samples. The high stability of the electrodes can be shown by the decline of just 3% of the photocurrent performance over three CLV measurements. Measurements in an alternative H_2SO_4 electrolyte exhibit a remarkable performance up to a maximum value of 3.3 mA cm^{-2} at 1.23 V_{RHE} without the application of any cocatalysts or any sacrificial agents. This photocurrent density corresponds to 82% percent of the theoretical maximum value for pure tungsten oxide photoelectrodes. These high photocurrent values can be reached due to the combination of porosity and the optimal layer thickness. While the porosity increases the number of active sites at the surface and increases the absorption by internal scattering and reflections, the optimal film thickness prevents a too high charge carrier recombination rate. For this reason, the performance of the photoelectrodes presented above exceeds that of comparable systems reported previously. However, due to the sub-optimal efficiency observed in the wavelength range below 400 nm, there is still scope for enhancement in these electrodes.

Our synthesis approach is highly reproducible, and the photoelectrodes exhibit high stability over the course of cycling photocurrent measurements, making this method a promising and easy synthesis of high-performing WO_3 photoanodes for manifold applications.

Acknowledgements

The authors thank Dr Jana Timm and Jonas Jungmann for the physisorption measurements and Dr Anja Hofmann for the SEM analysis. They also thank the Bavarian Polymer Institute (BPI, Keylab Electron and Optical Microscopy) for the possibility to utilize the SEM Zeiss Leo 1530. This work was supported by the Deutsche Forschungsgemeinschaft (DFG, German Research Foundation) within the CRC-1585 'Structured functional materials for multiple transport in nanoscale confinements', MultiTrans, project B02 (project number 492723217). R.M. acknowledges funding by the DFG in the Major Research Instrumentation funding program, project INST 91/459-1 (project no. 468685973).

Open Access funding enabled and organized by Projekt DEAL.

Conflict of Interest

The authors declares no conflict of interest.

Data Availability Statement

The data that support the findings of this study are available from the corresponding author upon reasonable request.

Keywords: mesoporous · photoelectrochemistry · tungsten oxide · water splittig

[1] H. R. V. Samborska, *Wildfires*, https://ourworldindata.org/wildfires (accessed: August 2024).
[2] V. Weilnhammer, J. Schmid, I. Mittermeier, F. Schreiber, L. Jiang, V. Pastuhovic, C. Herr, S. Heinze, *Int. J. Hyg. Environ. Health* **2021**, *233*, 113688.
[3] L. Tarasova, D. Lun, R. Merz, G. Blöschl, S. Basso, M. Bertola, A. Miniussi, O. Rakovec, L. Samaniego, S. Thober, R. Kumar, *Commun. Earth Environ.* **2023**, *4*, 1.
[4] G. Naumann, C. Cammalleri, L. Mentaschi, L. Feyen, *Nat. Clim. Chang.* **2021**, *11*, 485.
[5] P. P. Edwards, V. L. Kuznetsov, W. I. F. David, *Philos. Trans. R. Soc. A* **2007**, *365*, 1043.
[6] Y. Yang, S. Niu, D. Han, T. Liu, G. Wang, Y. Li, *Adv. Energy Mater.* **2017**, *7*, 1700555.
[7] L. J. Minggu, W. R. W. Daud, M. B. Kassim, *Int. J. Hydrogen Energy* **2010**, *35*, 5233.
[8] C. Acar, I. Dincer, *Int. J. Hydrogen Energy* **2016**, *41*, 7950.
[9] I. R. Hamdani, A. N. Bhaskarwar, *Renewable Sustainable Energy Rev.* **2021**, *138*, 110503.
[10] A. Vilanova, P. Dias, T. Lopes, A. Mendes, *Chem. Soc. Rev.* **2024**, *53*, 2388.
[11] K. Honda, A. Fujishima, *Nature* **1972**, *7*, 37.
[12] F. E. Osterloh, B. A. Parkinson, *MRS Bull.* **2011**, *36*, 17.
[13] O. Monfort, L. C. Pop, S. Sfaelou, T. Plecenik, T. Roch, V. Dracopoulos, E. Stathatos, G. Plesch, P. Lianos, *Chem. Eng. J.* **2016**, *286*, 91.
[14] M. Rohloff, B. Anke, S. Zhang, U. Gernert, C. Scheu, M. Lerch, A. Fischer, *Sustainable Energy Fuels* **2017**, *1*, 1830.
[15] P. S. Shinde, S. Y. Lee, S. H. Choi, H. H. Lee, J. Ryu, J. S. Jang, *Sci. Rep.* **2016**, *6*, 32436.
[16] R. Jia, Y. Wang, A. Li, C. Cheng, *Mater. Chem. Front.* **2023**, *8*, 1230.
[17] R. Abdullah, A. A. Jalil, M. Asmadi, N. S. Hassan, M. B. Bahari, M. Alhassan, N. M. Izzudin, M. H. Sawal, R. Saravanan, H. Karimi-Maleh, *Int. J. Hydrogen Energy* **2024**, *107*, 183.
[18] M. Ma, Y. Huang, J. Liu, K. Liu, Z. Wang, C. Zhao, S. Qu, Z. Wang, *J. Semicond.* **2020**, *41*, 091702.
[19] M. M. Abouelela, G. Kawamura, A. Matsuda, *J. Energy Chem.* **2022**, *73*, 189.
[20] G. Liu, S. Ye, P. Yan, F. Xiong, P. Fu, Z. Wang, Z. Chen, J. Shi, C. Li, *Energy Environ. Sci.* **2016**, *9*, 1327.
[21] B. S. Kalanoor, H. Seo, S. S. Kalanur, *Mater. Sci. Energy Technol.* **2018**, *1*, 49.
[22] M. B. Costa, M. A. de Araújo, M. V. D. L. Tinoco, J. F. d. Brito, L. H. Mascaro, *J. Energy Chem.* **2022**, *73*, 88.
[23] G. Zheng, J. Wang, H. Liu, V. Murugadoss, G. Zu, H. Che, C. Lai, H. Li, T. Ding, Q. Gao, Z. Guo, *Nanoscale* **2019**, *11*, 18968.
[24] Z. Ni, Q. Wang, Y. Guo, H. Liu, Q. Zhang, *Catalysts* **2023**, *13*, 579.
[25] T. Singh, R. Müller, J. Singh, S. Mathur, *Appl. Surf. Sci.* **2015**, *347*, 448.
[26] X. Liu, F. Wang, Q. Wang, *Phys. Chem. Chem. Phys.* **2012**, *14*, 7894.
[27] S. A. Alves, L. L. Soares, L. A. Goulart, L. H. Mascaro, *J. Solid State Electrochem.* **2016**, *20*, 2461.
[28] J. C. Hill, K. S. Choi, *J. Phys. Chem. C.* **2012**, *116*, 7612.
[29] S. Wang, H. Chen, G. Gao, T. Butburee, M. Lyu, S. Thaweesak, J.-H. Yun, A. Du, G. Liu, L. Wang, *Nano Energy* **2016**, *24*, 94.
[30] Y. Pihosh, I. Turkevych, K. Mawatari, J. Uemura, Y. Kazoe, S. Kosar, K. Makita, T. Sugaya, T. Matsui, D. Fujita, M. Tosa, M. Kondo, T. Kitamori, *Sci. Rep.* **2015**, *5*, 11141.
[31] M. Altomare, N. T. Nguyen, A. Naldoni, R. Marschall, *Photoelectrocatalysis*, Elsevier, Amsterdam, Netherlands **2023**, pp. 83–174.
[32] C. R. Lhermitte, N. Plainpan, P. Canjura, F. Boudoire, K. Sivula, *RSC Adv.* **2020**, *11*, 198.

[33] S. S. Kalanur, H. Seo, *J. Colloid Interface Sci.* **2018**, *509*, 440.
[34] Y. Ma, Y. H. Hu, *Appl. Phys. Lett.* **2021**, *118*, 209901.
[35] Q. Chen, J. Li, B. Zhou, M. Long, H. Chen, Y. Liu, W. Cai, W. Shangguan, *Electrochem. Commun.* **2012**, *20*, 153.
[36] N. A. Anuar, M. A. Mohamed, N. S. N. Hasnan, W. N. A. W. Mokhtar, M. N. I. Salehmin, L. J. Minggu, M. S. Mastuli, M. B. Kassim, *Int. J. Hydrogen Energy* **2024**, *51*, 476.
[37] A. Kaur, B. Bajaj, A. Kaushik, A. Saini, D. Sud, *Mater. Sci. Eng. B* **2022**, *286*, 116005.
[38] Y. Zi, Y. Hu, J. Pu, M. Wang, W. Huang, *Small* **2023**, *19*, 2208274.
[39] Y. Wang, F. Zhang, M. Yang, Z. Wang, Y. Ren, J. Cui, Y. Zhao, J. Du, K. Li, W. Wang, D. J. Kang, *Microporous Mesoporous Mater.* **2019**, *284*, 403.
[40] W. Li, J. Liu, D. Zhao, *Nat. Rev. Mater.* **2016**, *1*, 16023.
[41] Y. Xie, D. Kocaefe, C. Chen, Y. Kocaefe, *J. Nanomater.* **2016**, *2016*, 2302595.
[42] S. Hilliard, G. Baldinozzi, D. Friedrich, S. Kressman, H. Strub, V. Artero, C. Laberty-Robert, *Sustainable Energy Fuels* **2017**, *1*, 145.
[43] H. Dotan, K. Sivula, M. Grätzel, A. Rothschild, S. C. Warren, *Energy Environ. Sci.* **2011**, *4*, 958.
[44] S. S. Kalanur, L. T. Duy, H. Seo, *Top. Catal.* **2018**, *61*, 1043.
[45] M. S. Amer, P. Arunachalam, A. M. Al-Mayouf, S. Prasad, M. N. Alshalwi, M. A. Ghanem, *Nanomaterials* **2019**, *9*, 1502.
[46] Y. Wang, W. Tian, C. Chen, W. Xu, L. Li, *Adv. Funct. Mater.* **2019**, *29*, 1809036.
[47] A. G. M. Popescu, I. V. Tudose, C. Romanitan, M. Popescu, M. Manica, P. Schiopu, M. Vladescu, M. P. Suchea, C. Pachiu, *Nanomaterials* **2024**, *14*, 141227.
[48] W. Song, R. Zhang, X. Bai, Q. Jia, H. Ji, *J. Mater. Sci. Mater. Electron.* **2020**, *31*, 610.
[49] S. Balaji, Y. Djaoued, A. S. Albert, R. Brüning, N. Beaudoin, J. Robichaud, *J. Mater. Chem.* **2011**, *21*, 3940.
[50] Y. Spectroscopies, Y. Shigesato, A. Murayama, T. Kamimori, K. Matsuhiro, *Appl. Surf. Sci.* **1988**, *33*, 811.
[51] J. Diaz-Reyes, A. Perez-Benitez, J. A. Balderas-López, J. Díaz-Reyes, J. A. Balderas-López, *Superf. Vacio* **2008**, *21*, 12.
[52] S. Ramkumar, G. Rajarajan, *Appl. Phys. A* **2017**, *123*, 401.
[53] L. Giancaterini, S. M. Emamjomeh, A. De Marcellis, E. Palange, C. Cantalini, *Proc. Eng.* **2015**, *120*, 791.
[54] S. Badilescu, P. V. Ashrit, *Solid State Ion.* **2003**, *158*, 187.
[55] K. M. Ryan, T. Bala, R. D. Gunning, M. Venkatesan, J. F. Godsell, S. Roy, *Nanotechnology* **2009**, *20*, 415603.
[56] C. Santato, M. Ulmann, J. Augustynski, *Adv. Mater.* **2001**, *13*, 511.
[57] J. K. Kim, K. Shin, S. M. Cho, T. W. Lee, J. H. Park, *Energy Environ. Sci.* **2011**, *4*, 1465.
[58] M. Yagi, S. Maruyama, K. Sone, K. Nagai, T. Norimatsu, *J. Solid State Chem.* **2008**, *181*, 175.
[59] H. Chen, J. Li, W. Yang, S. E. Balaghi, C. A. Triana, C. K. Mavrokefalos, G. R. Patzke, *ACS Catal.* **2021**, *11*, 7637.
[60] Y. Li, Z. Liu, J. Li, M. Ruan, Z. Guo, *J. Mater. Chem. A* **2020**, *8*, 6256.
[61] M. Ade, L. Schumacher, R. Marschall, *Sustainable Energy Fuels* **2023**, *7*, 4332.
[62] J. A. Seabold, K.-S. Choi, *Chem. Mater.* **2011**, *23*, 1105.

Manuscript received: June 27, 2025
Version of record online: July 23, 2025